atmosphere

MDPI

Article

Characterization of Chemical Components and Optical Properties of Toluene Secondary Organic Aerosol in Presence of Ferric Chloride Fine Particles

Weichao Wang [1], Mingqiang Huang [1,*], Huimin Hu [1], Weixiong Zhao [2], Changjin Hu [2], Xuejun Gu [2] and Weijun Zhang [2,*]

[1] Fujian Province Key Laboratory of Modern Analytical Science and Separation Technology, College of Chemistry & Chemical Engineering and Environment, Minnan Normal University, Zhangzhou 363000, China; wangweichao980502@163.com (W.W.); huhuimin215@163.com (H.H.)

[2] Laboratory of Atmospheric Physico-Chemistry, Anhui Institute of Optics and Fine Mechanics, Chinese Academy of Sciences, Hefei 230031, China; wxzhaoaiofm@gmail.com (W.Z.); hucjaiofm@gmail.com (C.H.); xjguaiofm@gmail.com (X.G.)

* Correspondence: huangmingqiang@mnnu.edu.cn (M.H.); wjzhangaiofm@gmail.com (W.Z.); Tel.: +86-596-2591-445 (M.H.); Fax: +86-596-2026-037 (M.H.)

Abstract: Iron ion is the common transition metal ion in atmospheric aerosol, which can affect the components and optics of secondary organic aerosol (SOA). In the current study, the atmospheric photooxidation of toluene to produce SOA in the presence of ferric chloride fine particles is simulated in a smog chamber; on-line and off-line mass spectrometry and spectroscopic instruments are used to characterize constituents and optics of SOA. Compare with SOA formed in the absence of fine particles, the laser desorption/ionization mass spectra of toluene SOA generated in the presence of ferric chloride fine particles show ion peaks of m/z = 163 and 178, the UV-Vis spectra of the extracting solution for toluene SOA have peaks near 400 and 700 nm, and the electrospray ionization mass spectra contain peaks at m/z = 248 and 300. Based on this spectral information, it is shown that gaseous methylcatechol formed from photooxidation of toluene may react with iron ion on the surface of fine particles by complexing and oxidation–reduction, resulting in methylbenzoquinone products and metallo-organic complex ions such as $[Fe(III)(CH_3C_6H_3OO)]^+$, $[Fe(III)(CH_3C_6H_3\ OO)_2]^-$ and $[Fe(III)(CH_3C_6H_3OO)Cl_2]^-$. These products have strong light absorption ability, resulting in an increase in the averaged mass absorption coefficient (<*MAC*>) in the 200~1000 nm range and the *MAC* at 365 nm (MAC_{365}) for toluene SOA, while <*MAC*> and MAC_{365} progressively increase with an increasing concentration of ferric chloride fine particles. These results serve as experimental references for the study of the formation mechanism and optical properties of metallo-organic complexes in atmospheric aerosol particles in regions experiencing high levels of fine particles of metal and automobile exhaust pollution.

Keywords: toluene; ferric chloride; secondary organic aerosol; metallo-organic complex; optical property

check for updates

Citation: Wang, W.; Huang, M.; Hu, H.; Zhao, W.; Hu, C.; Gu, X.; Zhang, W. Characterization of Chemical Components and Optical Properties of Toluene Secondary Organic Aerosol in Presence of Ferric Chloride Fine Particles. *Atmosphere* **2023**, *14*, 1075. https://doi.org/10.3390/atmos14071075

Academic Editor: Petros N. Vasilakos

Received: 18 April 2023
Revised: 10 June 2023
Accepted: 21 June 2023
Published: 26 June 2023

Copyright: © 2023 by the authors. Licensee MDPI, Basel, Switzerland. This article is an open access article distributed under the terms and conditions of the Creative Commons Attribution (CC BY) license (https://creativecommons.org/licenses/by/4.0/).

1. Introduction

Toluene, ethylbenzene, xylene and other aromatic compounds are common organic pollutants in the atmosphere [1,2] and important precursors of secondary organic aerosol (SOA) [3–5]. SOA can scatter and absorb solar radiation, decrease atmospheric visibility [6–10] and endanger human health [11,12]. The study of its formation mechanism and optical properties has attracted extensive attention. Fine particles of metal emitted by human sources are main components of inorganic fine particles in the atmosphere [13]. Metals in form of oxides, hydroxides and silicates are transformed into soluble metal ions through atmospheric chemical processes [14,15]. Fe, Cu, Zn and Mn are common transition metal ions in fine particles [16]. The large specific surface area of fine particles of

metal is conducive to the condensation and reaction of semi- and non-volatile compounds, and it can affect the yield and composition of SOA particles [17,18]. In addition, transition metal ions have catalytic and redox capabilities. As a bridge between laboratory research and field monitoring, a smog chamber can be used to simulate atmospheric conditions; it is thus an indispensable experimental device for exploring atmospheric chemical reactions. A smog chamber is often utilized to simulate the atmospheric chemical processes of volatile organic compounds [19–21]. Chu et al. [22–24] carried out photooxidation experiments of toluene using a smog chamber and found that $MnSO_4$ and $ZnSO_4$ fine particles can catalyze the photolysis of H_2O_2 to form OH radicals, which react with toluene to produce more products. These products are partitioned into particle phases, leading to an increase in the yield of SOA. On the contrary, when $FeSO_4$ particles exist in a system, gaseous oxidation products of toluene and other compounds condense on fine particles, and a redox reaction with Fe^{2+} generates volatile compounds, which decreases the yield of SOA.

It should be noted that some d, s and p orbitals in the valence electron layer of transition metal ions are empty orbitals, which can form metallo-organic complexes with oxygen and nitrogen atoms containing lone pair electrons in phenolic, carboxylic acids and nitro compounds via coordination bonds [25]. Carboxylic acids and phenolic compounds are common organics in atmospheric aerosol particles. After they lose hydrogen atoms, oxygen atoms containing lone pair electrons have strong complexation ability and can form stable metallo-organic complexes with Fe^{3+}, Cu^{2+} and other transition metal ions [26–28]. These metallo-organic complexes are fat-soluble and easily absorbed by the intestinal wall through the biofilm, as well as transferred into the cerebrovascular system, placenta and other organs. They have stronger biological toxicity than metal ions [29], which has an important impact on human health and the ecological environment and has attracted wide attention. In addition, metallo-organic complexes contain double bonds and other chromophores, which can absorb light radiation and generate $\pi \rightarrow \pi^*$ or $n \rightarrow \pi^*$ transitions. Meanwhile, transition metal ions have d orbitals with unfilled electrons. Under the influence of a ligand field, d orbitals with the same energy as the original orbitals will split. After splitting, there is an energy difference between d orbitals, and the absorbed radiation can undergo d→d transition [30]. Therefore, metallo-organic complexes have strong absorption capacity in the ultraviolet and visible range, and they make a greater contribution to atmospheric light radiation. However, there are few reports of the effect of metal particles on the optical properties of SOA.

Iron ion is a common transition metal ion in atmospheric aerosol particles. It plays a crucial role in the aging of aerosols and the formation of brown carbon. Al-Abadleh addressed the current state of knowledge on iron chemistry that leads to SOA formation. She provided a detailed overview of the oxidation–reduction and complexation reactions of catechol, guaiacol and other polyhydroxyphenols, along with dicarboxylic acids such as oxalic acid and malonic acid, with iron ion to produce soluble and insoluble brown carbon products [31]. With the extensive use of fossil fuels in China, urban $PM_{2.5}$ contains a relatively high concentration of iron and other metal ions [32]. To date, the highest concentrations of soluble iron in $PM_{2.5}$ particles in Beijing have been 116.3 $ng \cdot m^{-3}$ and 308.9 $ng \cdot m^{-3}$ in summer and winter, respectively [33]. Toluene is the most highly concentrated aromatic compound and the main precursor of anthropogenic SOA [3,4]. Recently, our group has used a smog chamber to study the photooxidation reaction of toluene initiated by OH radicals. The chemical components of SOA were measured using an aerosol laser time-of-flight mass spectrometer (ALTOFMS) in real-time, and constituents such as cresol, methylcatechol and carbonyl compounds were obtained [34,35]. In addition, the single-scattering albedo of toluene SOA in the presence of 300 $\mu g \cdot m^{-3}$ ammonium sulfate fine particles was measured to be 0.81 ± 0.02 at λ = 470 nm [36]. Against that research background, in this study, on-line and off-line detection instruments are utilized to characterize the chemical components and optics of toluene SOA formed in the absence and presence of ferric chloride fine particles, as well as to identify metallo-organic complexes.

Furthermore, the influence of different concentrations of ferric chloride fine particles on the generation of metallo-organic complexes and the optical properties of toluene SOA is also explored. The findings provide experimental references for studying the formation and optics of metallo-organic complexes in atmospheric aerosol particles containing transition metal ions.

2. Experiments

2.1. Materials

Toluene (>99.7%) was purchased from Aladdin Reagent (Shanghai) Co., Ltd. (Shanghai, China). Methanol (>99%) and anhydrous ferric chloride (98%) were provided by Sigma Aldrich (Shanghai) Trading Co., Ltd. (Shanghai, China).

2.2. Smog Chamber Experiments

Experiments were performed in a homemade 850 L chamber [35,36]. The chamber device is mainly composed of a clean air generation system, inlet system, Teflon chamber and detection system. The Teflon chamber is made of an FEP-Teflon film, where one end of the film is sealed directly and the other end is sealed through a flange. The outer side of the flange is installed with injection and sampling tubes, while the inner side is equipped with a small fan to evenly mix the gas and particulate matter in the chamber. As shown in Figure 1, the relative humidity and temperature are detected by an HMT 333 sensor (Vaisala, Finland). According to our previous experimental results [36,37], the relative humidity (RH) of clean air generated by the air purification system is 25 ± 2%. Therefore, all experiments are carried out under the condition of RH = 25 ± 2%. Meanwhile, the temperature is controlled at 298 ± 1 K by the laboratory air conditioning system. Thus, the relative humidity and temperature are 25 ± 2% and 298 ± 1 K for each experiment. After cleaning the chamber, it is filled with about 150 L clean air, and then an aerosol generator (TSI 9302, Shoreview, MN, USA) is used to atomize 1 g·L^{-1} ferric chloride solution to produce fine particles with sizes of less than 2 μm, which are diffused through a silica gel drying tube and then entered into the chamber. A certain amount of toluene is sampled by a micro liter injector and delivered to a liquid gasification bottle heated to 353 K by a temperature-controlled heating sleeve. By doing so, it is volatilized into gas and expanded into a gas distribution system; then, it is entered into the chamber with clean air. Subsequently, ozone formed using an XM-TS ozone generator (Qingdao Xinmei Purification Equipment Co., Ltd., Qingdao China) is added to the gas distribution system, then introduced into the chamber with clean air. Finally, the chamber is filled to the full volume with clean air, and the reactants are evenly mixed with the help of small fan in the flange. Four ultraviolet lamps (characteristic wavelength of 254 nm) around the chamber are turned on to illuminate the ozone, generating OH radicals [38] and initiating the photooxidation reaction of toluene. An ozone analyzer (GT-1000-O3, Shenzhen Colno Electronic Technology Co., Ltd., Shenzhen, China, with flowrate of 0.50 L·min^{-1}), GC-FID (7820A, Agilent, Palo Alto, CA, USA, with flowrate of 0.04 L·min^{-1}) and scanning mobility particle size analyzer (SMPS, 3080L DMA, 3775 CPC, TSI, Shoreview, MN, USA, with flowrate of 0.30 L·min^{-1}) are successively adopted for on-line measurement of the concentrations of ozone, toluene and SOA particles in the chamber [35,36].

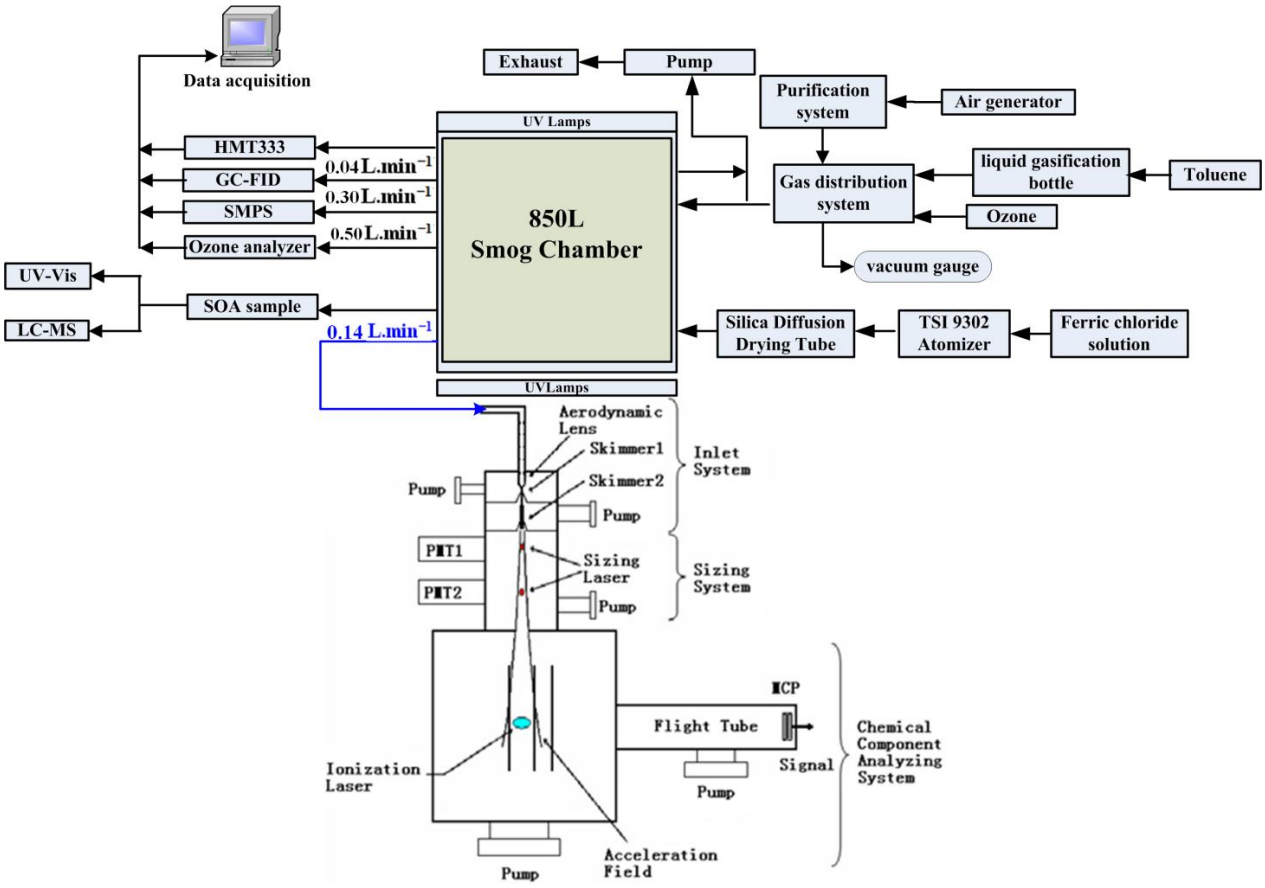


Figure 1. Diagram of combined device for ALTOFMS and smog chamber.

2.3. Characterization Components of Toluene SOA

Due to the small volume of the Teflon chamber (850 L), the concentration of aromatic hydrocarbon and oxidant in our previous experiments was about 1–20 ppm [35–37]. Although the concentrations of reactants in the chamber are higher than that in the ambient atmosphere, the results of our studies may be useful for SOA formation modeling in areas where automobile exhaust pollution is serious. Thus, the concentrations of ozone and toluene were set at 10 ppm and 1 ppm in this study. The particle number and mass concentration of ferric chloride fine particles generated by TSI 9302 and detected by SMPS were about 3.6×10^7 particle.cm^{-3} and 1400 μg·m^{-3}, respectively. The particle number and mass concentration of ferric chloride fine particles can be controlled by adjusting the inlet time. When the clean air was filled to full volume, the particle number concentration of ferric chloride fine particles was in the range of 3.9×10^5–5.5×10^6 particle.cm^{-3} in different experiments. Nine experiments were performed, and each experiment was carried out three times. The concentrations of ozone and toluene in each experiment remained unchanged (10 ppm and 1 ppm), while the concentration of ferric chloride fine particles was set at 0, 15, 30, 60, 90, 120, 150, 180 and 210 μg·m^{-3} in turn. The chemical components of toluene SOA were measured on-line by ALTOFMS after irradiation with a flowrate of 0.14 L·min^{-1}. As displayed in Figure 1, SOA particles sequentially pass through an aerodynamic lens, with two skimmers to form the collimated particle beam, and enter into a sizing system. Particle size is attained by measuring the transit time of particle travel through two infrared laser beams with a wavelength of 532 nm. Then, particles enter the ionization chamber, where they are desorbed and ionized by a 266 nm ultraviolet laser emitted by a Nd: YAG pulsed laser. The formed ions are measured by a time-of-flight mass spectrometer to obtain the mass spectrum of the particles [35–37].

Next, SOA particles are collected on a polytetra fluoroethylene membrane filter, and they are extracted into 5 mL of 2% (v/v) methanol water solution by ultrasound for 30 min.

UV-Vis spectra of the extracting solutions are detected by a UV-6100S spectrophotometer (Mapada Instruments, China). Moreover, the extracting solutions are measured with a high-performance liquid chromatography mass spectrometer (LC-MS) with electrospray ionization (ESI) (Agilent-1200, Agilent-6320, Palo Alto, CA, USA). The mobile phase is methanol and ultra-pure water (v/v = 1:1) at a flowrate of 0.20 μL·min^{-1}. Since no suitable chromatographic column was found to separate the metallo-organic complexes in this study, however, the negative ionization mode of electrospray ionization of LC-MS caused the organic molecules to dissociate hydrogen ions and produce a deprotonated molecular ion peak ([M-H]$^-$), which provided molecular weight information on the tested organic component [39]. This could be used for qualitative analysis of metallo-organic complexes and other components of the extracting solution for toluene SOA. Thus, the sample was measured with no chromatography column attached, and the extracting solution was electrospray ionized directly, then detected in the 50–1000 amu range of the negative mode [36]. Based on the detected deprotonated molecular ion peak ([M-H]$^-$), a qualitative analysis of metallo-organic complexes and other components was carried out.

2.4. Optical Characterization of Toluene SOA

Referring to experiments on SOA optical measurements [40,41] and our previous study [42], we characterized the optics of toluene SOA by using a mass absorption coefficient (*MAC*, cm^2·g^{-1}), which can be obtained according to Formula (1):

$$MAC(\lambda) = \frac{A^{solution}(\lambda) \times \ln 10}{b \times C_{mass}} \quad (1)$$

$$\langle MAC \rangle = \frac{1}{(\lambda_2 - \lambda_1)} \times \int_{\lambda_1}^{\lambda_2} MAC(\lambda) d\lambda \quad (2)$$

where $A^{solution}(\lambda)$ is the absorbance of the extracting solution for toluene SOA at λ, C_{mass} is the organic carbon concentration of the extracting solution (g·cm^{-3}) and b is the optical path (1 cm for this study). Meanwhile, the integral value of *MAC* over the measured wavelength range is divided by ($\lambda_2 - \lambda_1$) to obtain the averaged *MAC* (<*MAC*>, cm^2·g^{-1}) in the λ_1–λ_2 range (Formula (2)). The absorption spectra at 200–1000 nm and the organic carbon concentration of the extracting solution for toluene SOA particles are detected by a UV-6100s spectrometer and TOC-L organic carbon analyzer (Shimadzu, Japan), respectively [42]. The organic carbon concentration of the 2% methanol water solution is measured firstly by the TOC-L organic carbon analyzer. The organic carbon concentration (C_{mass}) of the extracting solution for toluene SOA is obtained by subtracting the organic carbon concentration of the 2% methanol water solution from the total organic carbon concentration that is detected [42]. Then, <*MAC*> of toluene SOA particles in the 200–1000 nm range is acquired via Formulas (1) and (2). *MAC* at 365 nm (MAC_{365}) is more commonly used in the literature [43–45]. Thus, by combining the absorbance at 365 nm ($A^{solution}$ (365 nm)) with the organic carbon concentration (C_{mass}), MAC_{365} of toluene SOA under different concentrations of ferric chloride fine particles is obtained through Formula (1). It should be pointed out that, regarding the above *MAC* calculation, the light absorption in the solution is ~2 times higher than that in the air owing to artifacts [46,47].

3. Results

3.1. Generation of Toluene SOA with and without Ferric Chloride Fine Particles

Experimental [36,48–50] and theoretical [51–53] results show that an addition reaction between toluene and OH radicals mainly occurs, producing methylhydroxycyclo hexadienyl radicals. As shown in Figure 2, an oxygen molecule extracts a hydrogen atom from the carbon atom connected with an OH radical to form cresol. The generated cresol can react with an OH radical and oxygen molecule to yield methylcatechol. In addition, a methylhydroxycyclohexadienyl radical can react with an oxygen molecule to produce a peroxy radical, and through a series of reactions, ring cracking may occur to form glyoxal

and other aldehydes. The resultant aldehydes continue to be oxidized by OH radicals to oxalic acid and other carboxylic acids [54]. These products achieve a saturated vapor pressure and then nucleate and condense to generate SOA particles.

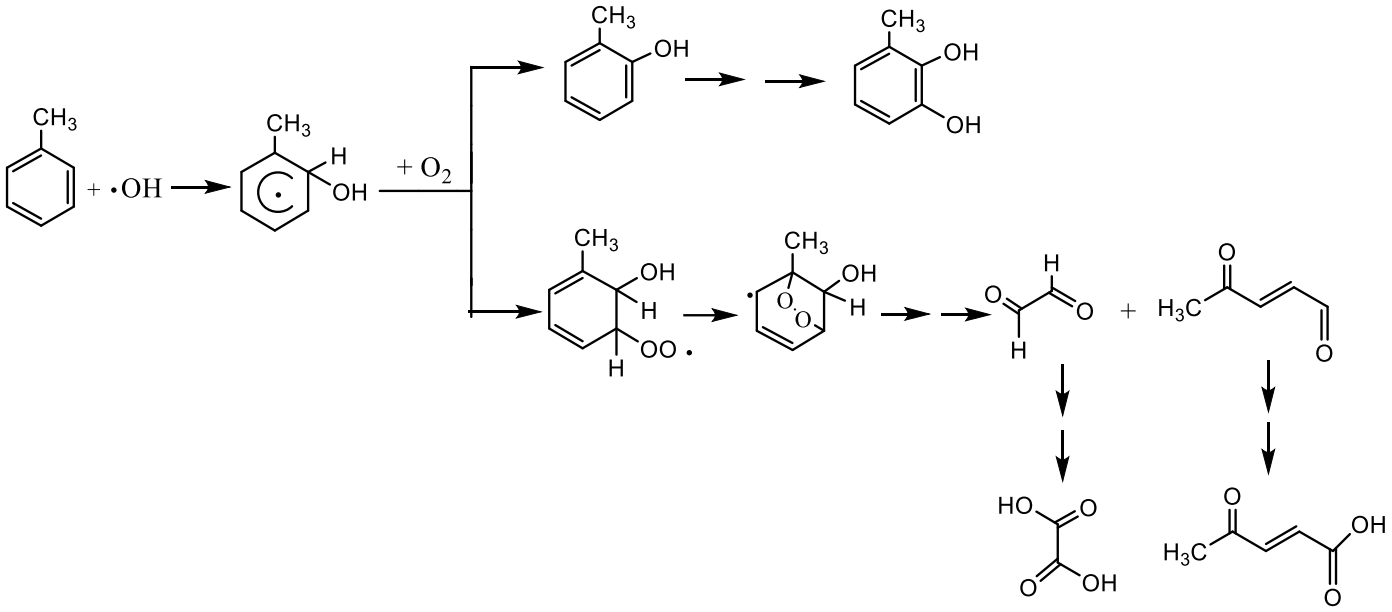


Figure 2. Suggested mechanism for phenolic and carbonyl compounds formed from OH-initiated oxidation of toluene.

SMPS is utilized to detect the concentration of SOA, and the wall effect is then corrected for in accordance with our previous studies [35,36]. Particle wall loss is defined as a first-order process dependent on particle loss coefficient, k_{dep} (d_p):

$$k_{dep}(d_p) = ad_p^b + c/d_p^d$$

where a, b, c and d are 4.17×10^{-13}, 4.66, 10.18 and 0.75, respectively [35–37]. The concentration of toluene SOA is corrected by fitting the particle number concentration decay at the end of each experiment. For the case of photooxidation of toluene in the absence of ferric chloride fine particles, as shown in Figure 3a, relative humidity during the irradiation process is maintained at 24–25%, and the temperature is between 298 and 300 K. The concentration of toluene and ozone decreases gradually with the extension of irradiation time (Figure 3b). The concentration of toluene SOA after wall effect correction as a function of irradiation time is shown in Figure 3b. A certain amount of toluene is consumed within 15 min so that products such as methylcatechol and glyoxal achieve saturated vapor pressure, meaning less SOA is generated and the concentration is only 6 $\mu g \cdot m^{-3}$. After that, the formation of gaseous products keeps increasing and the SOA concentration rises expeditiously, from 22 to 174 $\mu g \cdot m^{-3}$ within 30 to 150 min. The presence of toluene is not detected in the chamber at 180 min, and the SOA concentration attains a maximum value of 202 $\mu g \cdot m^{-3}$. Thereafter, due to the reaction of toluene being completed, methylcatechol, glyoxal and other products are no longer produced, and the corrected SOA concentration tends to stabilize [35,36].

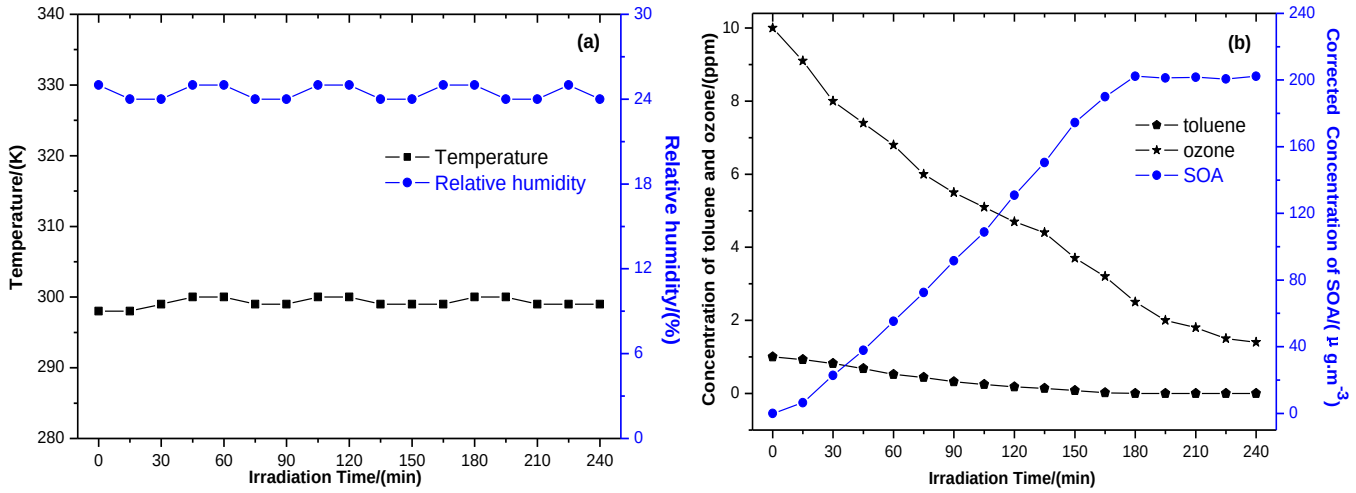


Figure 3. The relative humidity and temperature (**a**) and the concentrations of ozone, toluene and SOA after wall effect correction (**b**), all measured as a function of irradiation time in the absence of ferric chloride fine particles.

The variation curves of relative humidity, temperature, toluene and ozone consumption, as well as SOA formation with irradiation time throughout the experiments in the presence of ferric chloride fine particles, are analogous to those in the absence of fine particles shown in Figure 3. However, the formation concentration of toluene SOA increases to varying degrees when compared to that in the absence of fine particles. For example, in the presence of 120 $\mu g \cdot m^{-3}$ ferric chloride fine particles, as displayed in Figure 4, the concentration of toluene SOA as a function of time is higher than that in the absence of fine particles. The maximum concentration of SOA reaches 346 $\mu g \cdot m^{-3}$ at 180 min irradiation, which is about 71% higher than that in the absence of fine particles. In addition, the maximum concentration of SOA particles after wall effect correction, illustrated in Figure 5, is about 234–350 $\mu g \cdot m^{-3}$ under different concentrations of ferric chloride fine particles, which is larger than the maximum SOA concentration without fine particles (202 $\mu g \cdot m^{-3}$). These results indicate that ferric chloride fine particles can change the gas/particle partitioning process of toluene photooxidation products, so that more methylcatechol, glyoxal and other gaseous products are partitioned to the particulate phase, thus facilitating the generation of SOA particles. However, when the concentration of ferric chloride fine particles is greater than 120 $\mu g \cdot m^{-3}$, the maximum SOA concentration remains almost constant. For characterizing the components of toluene SOA, on-line mass spectrometry and off-line spectral determinations are carried out.

3.2. Chemical Constituents of Toluene SOA with and without Ferric Chloride Fine Particles

In order to facilitate comparison, the constituents of SOA without fine particles are detected on-line by ALTOFMS firstly. The averaged laser desorption/ionization positive ion mass spectra for 200 toluene SOA single particles are displayed in Figure 6. In addition to fragment peaks of organic carbon (m/z = 12 (C^+) and 24 (C_2^+)), there are characteristic fragment ion peaks of phenolic substances (m/z = 93, $C_6H_5O^+$), the benzene ring (m/z = 77, $C_6H_5^+$) and its fragment peaks (m/z = 65, $C_5H_5^+$ and m/z = 39, $C_3H_3^+$), demonstrating the presence of phenolic compounds in SOA particles [37,55]. In addition, mass spectra show characteristic peaks of carbonyl compounds at m/z = 29 (HCO^+), 43 (CH_3CO^+) and 57 ($HCOCO^+$) [37,55], which indicate that toluene SOA particles contain carbonyl compounds. UV-visible absorption spectra of the extracting solution for toluene SOA particles without fine particles, displayed in Figure 7, have a strong peak at 210 nm, which represents characteristic absorption generated by the $n \rightarrow \pi^*$ transition of C=O [39]. Furthermore, there is an absorption band near 277 nm, which corresponds to the characteristic absorption of

phenolic substances [56]. These confirm again that phenolic and carbonyl compounds are principal constituents of toluene SOA.

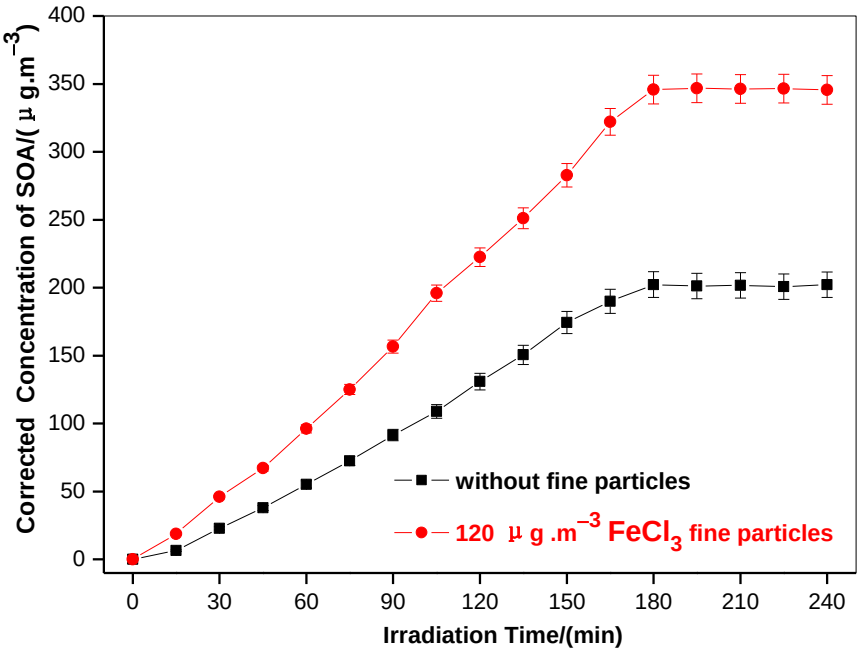


Figure 4. Concentration of SOA after wall effect correction as a function of time with and without 120 μg·m^{-3} ferric chloride fine particles.

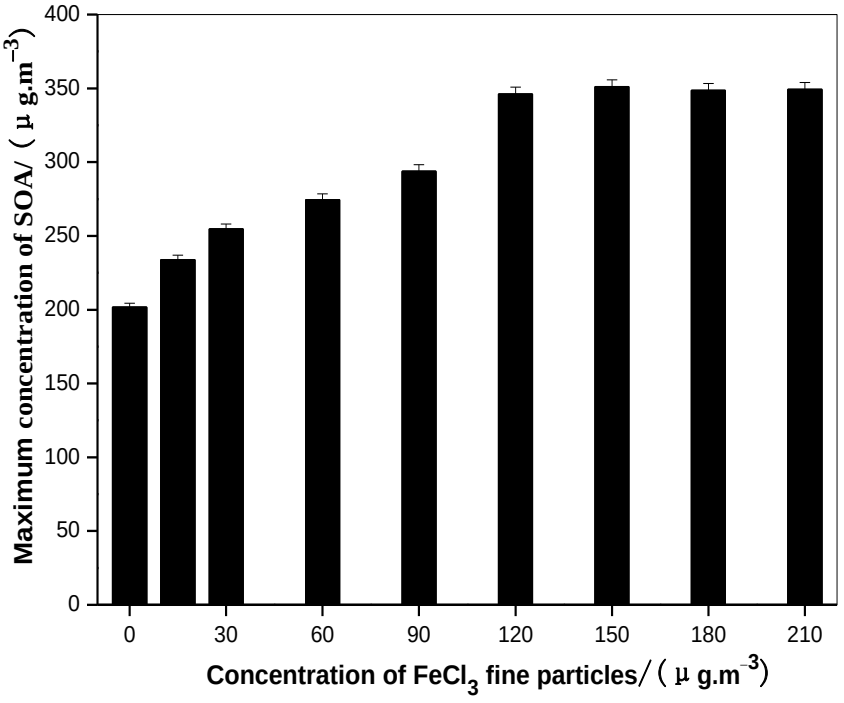


Figure 5. Maximum concentration of SOA after wall effect correction under different concentrations of ferric chloride fine particles.

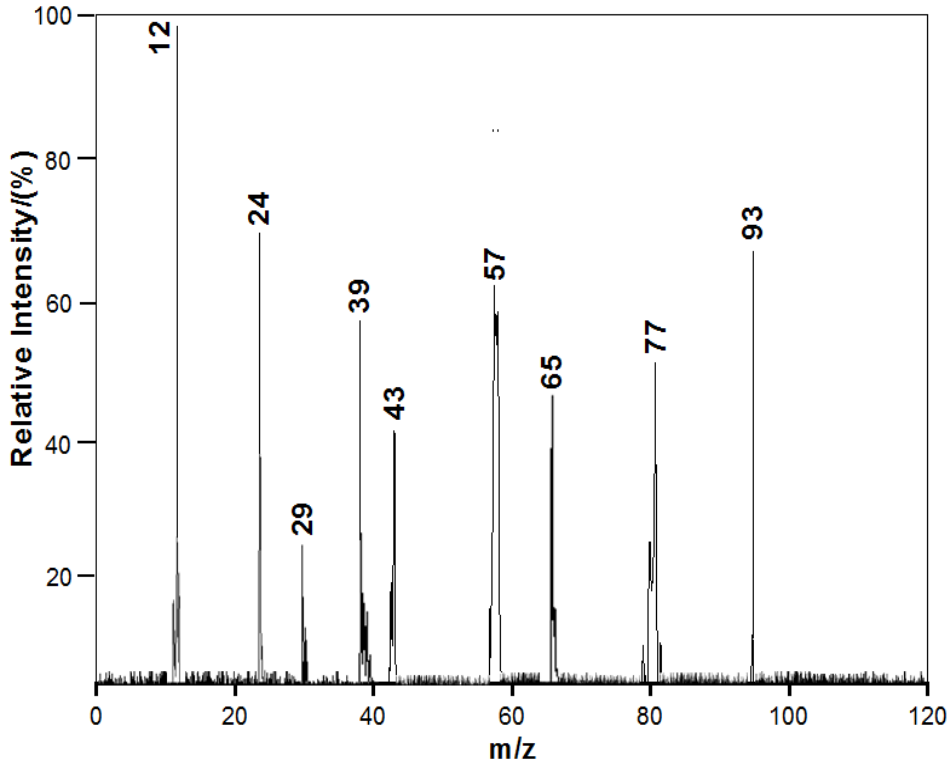


Figure 6. Averaged laser desorption/ionization positive ion mass spectra of 200 toluene SOA particles without ferric chloride fine particles.

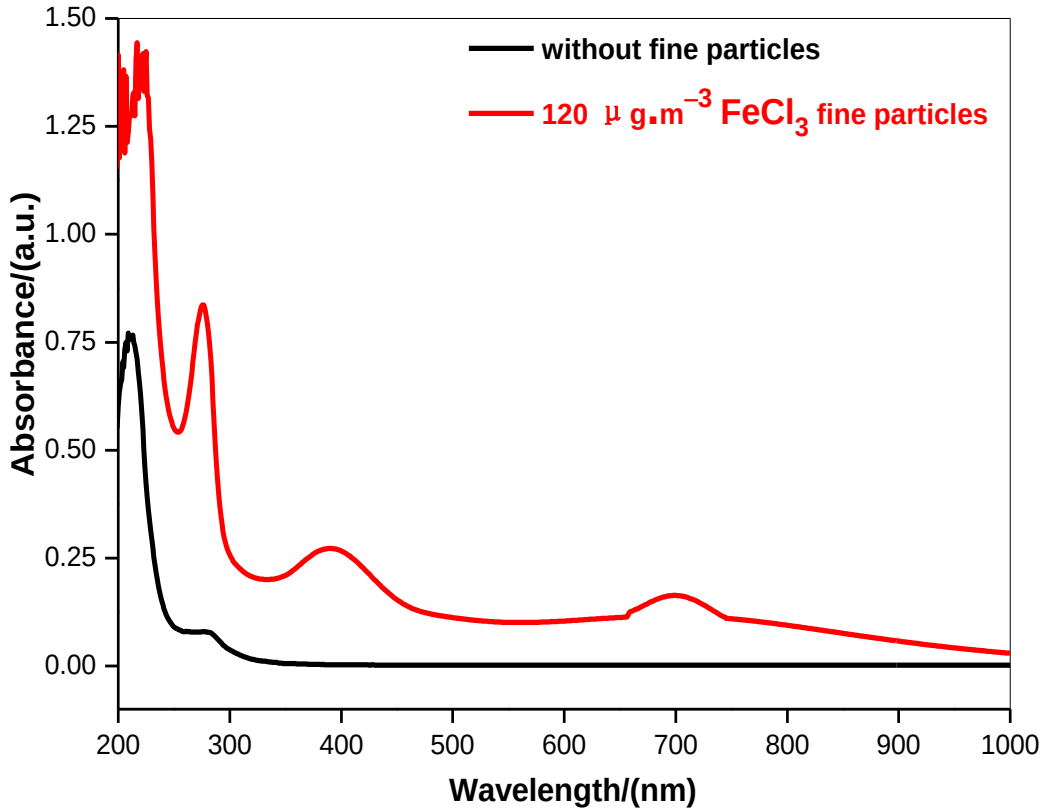


Figure 7. UV-Vis spectra of extracting solution for toluene SOA with and without 120 μg·m^{-3} ferric chloride fine particles.

The presence of phenolic and carbonyl products is reconfirmed by electrospray ionization mass spectra of the extracting solution for toluene SOA without fine particles. The negative ionization mode of electrospray ionization causes organic molecules to dissociate hydrogen ions and produces a deprotonated molecular ion peak ([M-H]$^-$), which provides molecular weight information on the tested organic component [39]. As displayed in Figure 8, electrospray ionization negative ion mass spectra contain [M-H]$^-$ ion peaks of m/z 57, 71, 89, 107, 123 and 139. Based on the possible reaction mechanism of toluene with OH radical and molecular weight (*Mw*) information, these ion peaks correspond to carbonyl and phenolic products, for example, glyoxal (*Mw* = 58, m/z = 57), methylglyoxal (*Mw* = 72, m/z = 71), oxalic acid (*Mw* = 90, m/z = 89), 2-methyl-2,3-epoxy-butanedial (*Mw* = 98, m/z = 97), cresol (*Mw* = 108, m/z = 107), methylcatechol (*Mw* = 124, m/z = 123) and methylpyrogallol (*Mw* = 140, m/z = 139). These results are consistent with previous chamber experiments [36,48–50], which detected cresol, methylcatechol, glyoxal, oxalic acid and other products in toluene SOA particles.

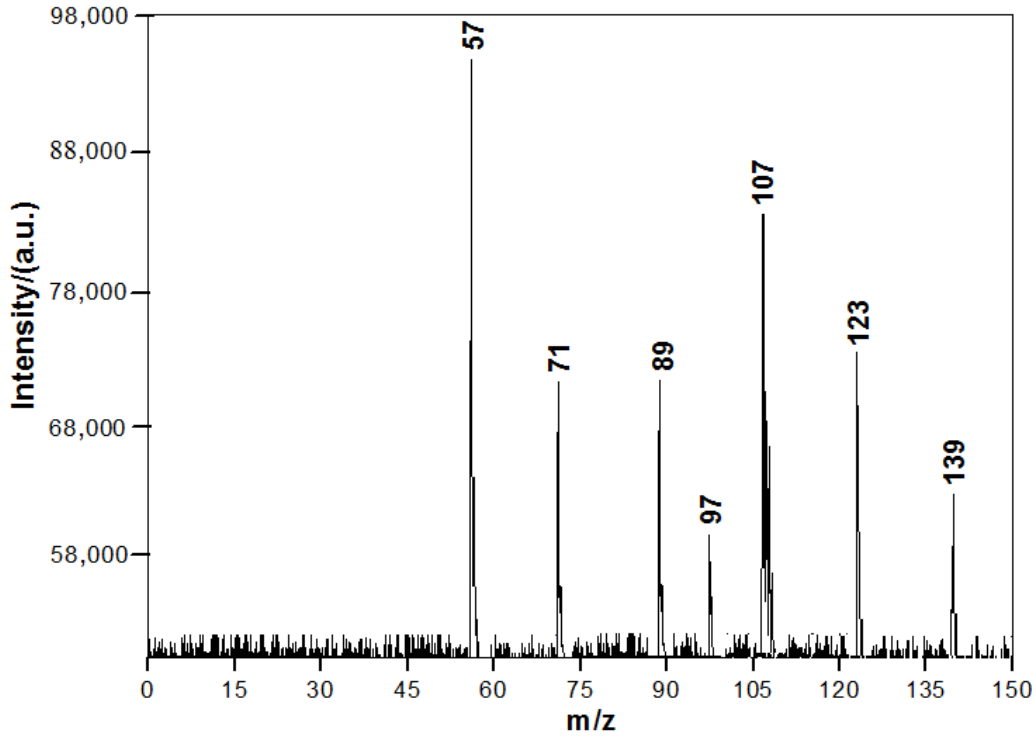


Figure 8. Electrospray ionization negative ion mass spectra of extracting solution for toluene SOA without ferric chloride fine particles.

It should be pointed out that, due to the limitation of data processing software, it is currently not possible to obtain differential mass spectra for quantitative analysis. However, based on the laser desorption/ionization positive ion mass spectra and electrospray ionization negative ion mass spectra of toluene SOA particles measured by ALTOFMS and LC-MS, the difference in mass peaks was qualitatively analyzed to illustrate the effect of ferric chloride fine particles on the photooxidation products of toluene and confirm the components of metallo-organic complexes. In the presence of 120 μg·m^{-3} ferric chloride fine particles, the averaged laser desorption/ionization positive ion mass spectra of 200 toluene SOA single particles were detected by ALTOFMS, as illustrated in Figure 9. The peak intensity of m/z = 56 in the spectra is the largest, corresponding to the mass peak of Fe^+ ions, while the strong intensity of m/z = 72 represents the FeO^+ ion peak [57]. In addition to organic carbon fragment peaks (m/z = 12, 24), carbonyl compound fragment peaks (m/z = 29, 43), a phenolic compound characteristic peak (m/z = 93), benzene ion and its fragment peak (m/z = 77, 65, 39), in this study, peaks of m/z = 107, 122,

164 and 178 with high intensity are newly present. The peak with m/z = 122 can probably be identified as a $CH_3C_6H_3O_2^+$ ion peak formed from the loss of two hydrogen atoms from the methylcatechol molecular ion, and we propose that m/z = 107 ($C_6H_3O_2^+$ ion) is generated by the loss of a methyl group from the $CH_3C_6H_3O_2^+$ ion. Moreover, the peak of m/z = 178 probably corresponds to a double dentate mononuclear methylcatechol iron ([Fe(III)(CH_3 C_6H_3OO)]$^+$) peak, and we propose that m/z = 163 is an ion peak generated when [Fe(III)($CH_3C_6H_3OO$)]$^+$ ion loses its methyl group ([Fe(III) (C_6H_3OO)]$^+$ ion).

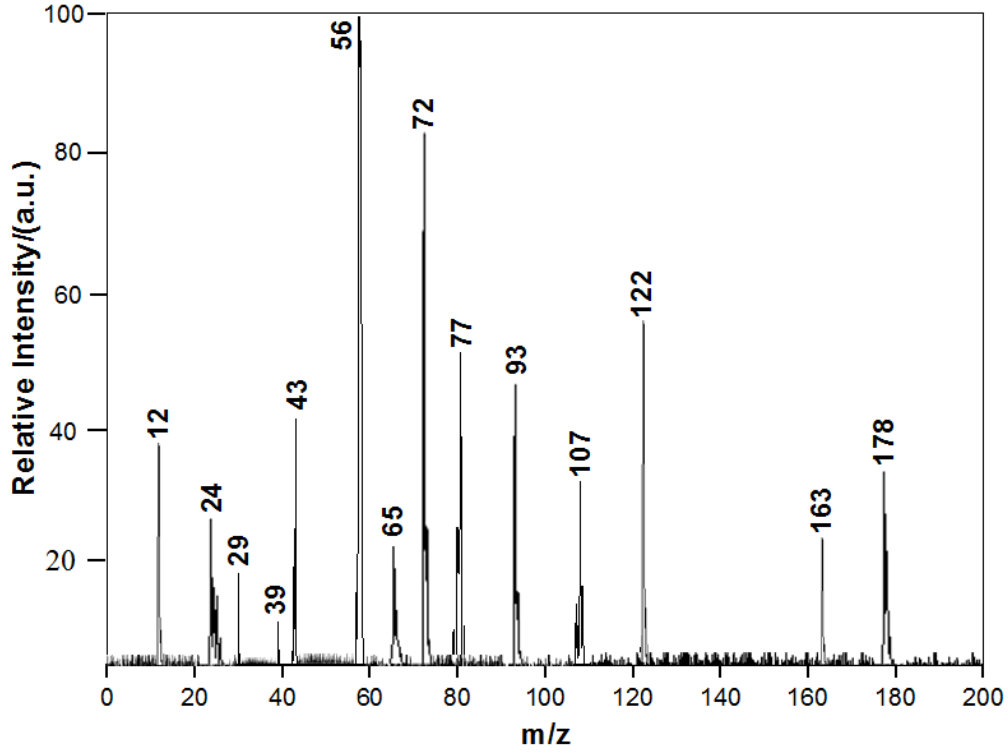


Figure 9. Averaged laser desorption/ionization positive ion mass spectra of 200 toluene SOA particles with 120 μg·m^{-3} ferric chloride fine particles.

Rizvi et al. [58] showed that a low-spin (t_2g_5) octahedron configuration of Fe (III) is a hard cation occupying a single π symmetric t_2g_5 orbital. According to matching hard–hard interaction, harder donor site (such as negatively charged oxygen) ligands can bind Fe (III) more strongly. According to the review of Al-Abadleh [31], catechol, guaiacol and other polyhydroxyphenols are common organic ligands. After catechol is dissolved in water and loses hydrogen ions, the two oxygen atoms are negatively charged and complexed with Fe(III) to produce catechol iron (III) ion ([Fe(III)(C_6H_4OO)]$^+$). When ferric chloride fine particles exist in the reaction system, due to its strong moisture absorption capacity, Fe^{3+} and Cl^- ions are generated after surface moisture absorption. As shown in Figure 10, gaseous methylcatechol formed from toluene photooxidation condenses on the surface of fine particles, and it may undergo the reaction proposed by Al-Abadleh [31] to generate metallo-organic complex ions. After methylcatechol dissolves in the hygroscopic surface of ferric chloride fine particles and loses hydrogen ions, two oxygen atoms are negatively charged and complexed with Fe(III) to generate methylcatechol iron (III) ion ([Fe(III)(CH_3 C_6H_3OO)]$^+$).

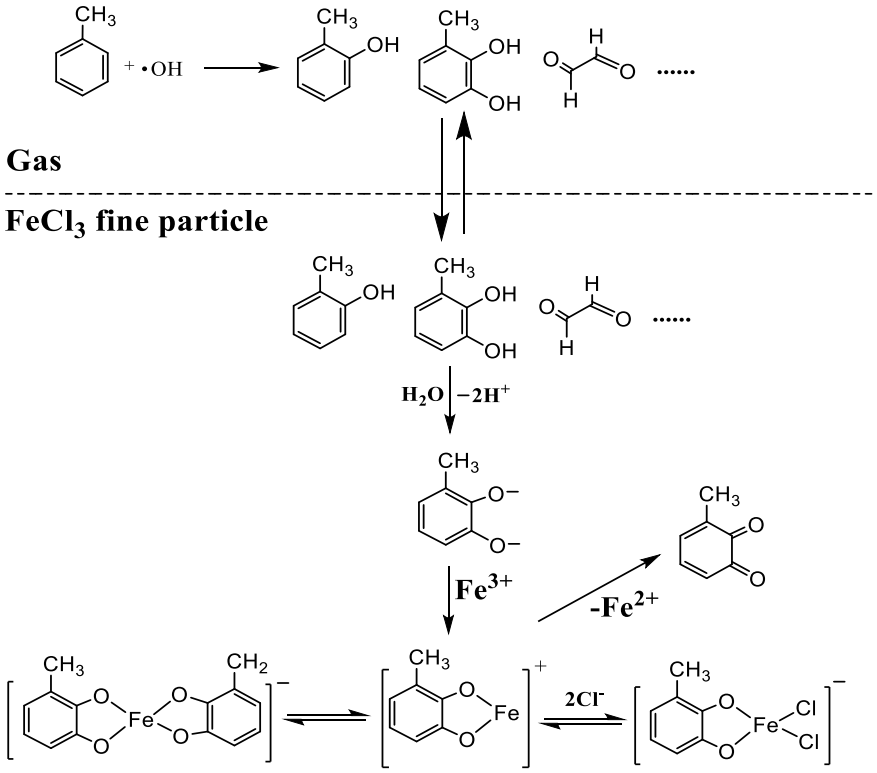


Figure 10. Possible mechanism of metallo-organic complex ions generated by photooxidation of toluene with ferric chloride fine particles.

UV-Vis spectra of the extracting solution for toluene SOA with 120 μg·m^{-3} ferric chloride fine particles further confirmed the existence of methylcatechol iron (III) ion. As shown in Figure 7, in addition to characteristic absorption peaks of carbonyl and phenolic compounds at 210 nm and 277 nm, new absorption peaks appeared near 400 nm and 700 nm. As suggested by Albarran et al. [59], the absorption peak at 400 nm is a characteristic peak formed from the $n \rightarrow \pi^*$ transition of benzoquinone molecules. This indicates the presence of benzoquinone products in the extracting solution. Powell et al. [60] and Slikboer et al. [61] have also observed an absorption peak near 700 nm when conducting an aqueous reaction of catechol and other phenolic compounds with an Fe (III) ion. On the basis of their analysis, it seems this peak is characteristic absorption resulting from charge transfer between a ligand and metal in the catechol–iron (III) ion. UV-Vis spectra of the extracting solution in this experiment, displayed in Figure 7, also reveal the absorption peak of 700 nm, indicating that gaseous methylcatechol produced by photooxidation of toluene can condense on the surface of hygroscopic ferric chloride particles, and a similar aqueous reaction occurs to generate methylcatechol iron (III) ion.

As shown in Figure 11, in addition to mass peaks of m/z = 57 (glyoxal), m/z = 71 (methylglyoxal), m/z = 89 (oxalic acid), m/z = 97 (2-methyl-2,3-epoxy-butanedial), m/z = 107 (cresol) and m/z = 123 (methylcatechol) in electrospray ionization negative ion mass spectra of the extracting solution for toluene SOA in the presence of 120 μg·m^{-3} ferric chloride fine particles, peaks of m/z = 121, 248 and 300 are also newly detected. The peak of m/z = 121 probably represents the peak of the deprotonated molecular ion of methylbenzoquinone ($CH_3C_6H_3OO^-$) [59], while the peaks of m/z = 248 and 300 may be identified as metallo-organic complex ion peaks. As shown in Figure 10, methylcatechol dissolves in water and loses hydrogen ions to produce $CH_3C_6H_3OO^{2-}$ ion, which is complexed with Fe(III) to form methylcatechol iron (III) ion ($[Fe(III)(CH_3C_6H_3OO)]^+$). As suggested by Slikboer et al. [61], methylcatechol iron (III) ion undergoes a redox reaction with the action of an oxygen molecule to produce a ferrous ion and methylbenzoquinone. In addition, methylcatechol iron (III) ion can be further complexed with $CH_3C_6H_3OO^{2-}$

ion to generate dimethylcatechol iron (III) ion ($[Fe(III)(CH_3\ C_6H_3OO)_2]^-$) [62]. The mass charge ratio of this ion is 300, so it can be inferred that m/z = 300 corresponds to the peak of this metallo-organic complex ion. It is worth noting that Cl^- ion produced on the surface of ferric chloride fine particles after moisture absorption is also a common inorganic ligand, which can be complexed with Fe(III) in catechol iron (III) ion to form dichloromethylcatechol iron (III) ion ($[Fe(III)(CH_3C_6H_3OO)Cl_2]^-$) [62]. The mass/charge ratio of this complex ion is 248, and m/z = 248 (shown in Figure 11) can be identified as the ion peak of $[Fe(III)(CH_3C_6H_3OO)Cl_2]^-$. Based on the above on-line and off-line measurement analysis, gaseous methylcatechol formed from photooxidation of toluene can coagulate and react on the surface of hygroscopic ferric chloride fine particles to generate metallo-organic ions, such as methylcatechol iron (III) ion, dimethylcatechol iron (III) ion, dichloro-methylcatechol iron (III) ion and methylbenzoquinone products.

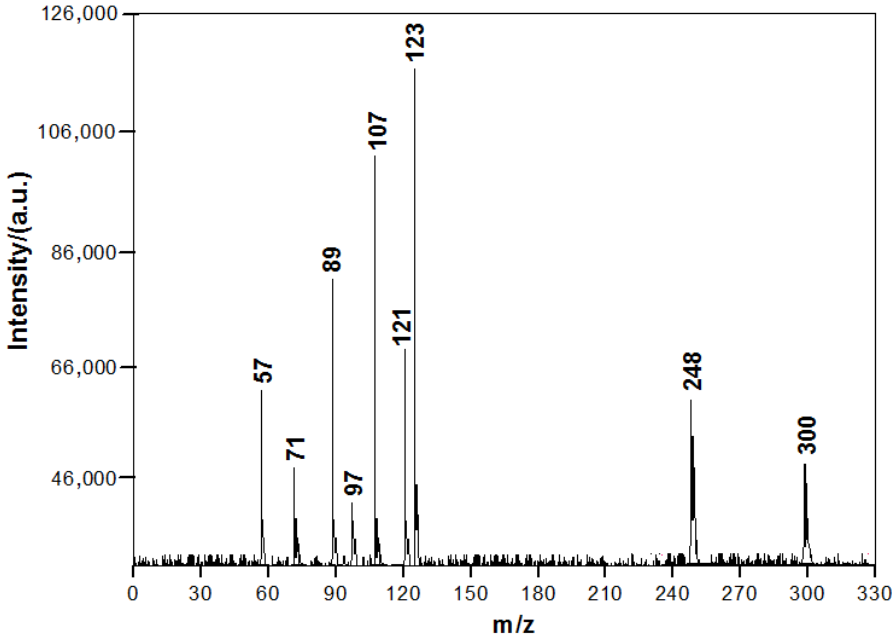


Figure 11. Electrospray ionization negative ion mass spectra of extracting solution for toluene SOA with 120 $\mu g \cdot m^{-3}$ ferric chloride fine particles.

3.3. MAC of Toluene SOA under Different Concentrations of Ferric Chloride Fine Particles

The specific surface of ferric chloride fine particles is the condensation center for gaseous products formed from photooxidation of toluene. The concentration of fine particles decides the size of the specific surface, which impacts the components and optical properties of SOA. <*MAC*> in the 200–1000 nm range and MAC_{365} of toluene SOA under ferric chloride fine particles with different concentrations were measured and the results are shown in Figures 12 and 13. The measured <*MAC*> of toluene SOA without fine particles is 178 $cm^2 \cdot g^{-1}$ (Figure 12), which is comparable to <*MAC*> of aromatic SOA reported by Updyke et al. [40] (200–300 $cm^2 \cdot g^{-1}$). Meanwhile, MAC_{365} of toluene SOA without fine particles is 407 $cm^2 \cdot g^{-1}$ (Figure 13), which is slightly higher than the value of aromatic SOA measured by Updyke et al. [40] (300–400 $cm^2 \cdot g^{-1}$), and less than the lower limit of 365 nm absorption values of water-soluble organic carbon (WSOC) in the outflow from northern China (2000–11,000 $cm^2 \cdot g^{-1}$) reported by Kirillova et al. [44]. The above test results show that methylcatechol and other phenolic compounds and carbonyl compounds such as glyoxal are the main constituents of toluene SOA without ferric chloride fine particles. These component molecules only have C=O and C=C double bonds, do not contain strong chromophores or auxochromes and have weak particle light absorption ability [43].

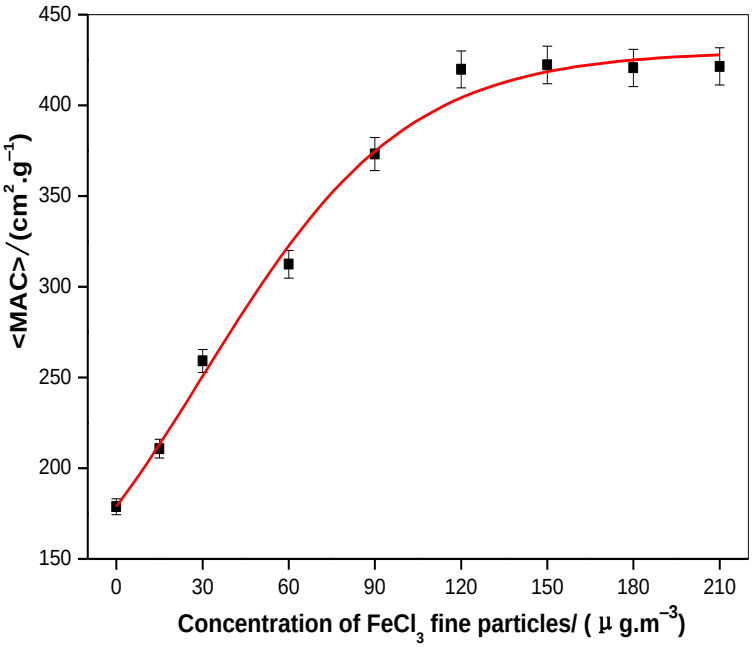


Figure 12. <*MAC*> of toluene SOA under different concentrations of ferric chloride fine particles.

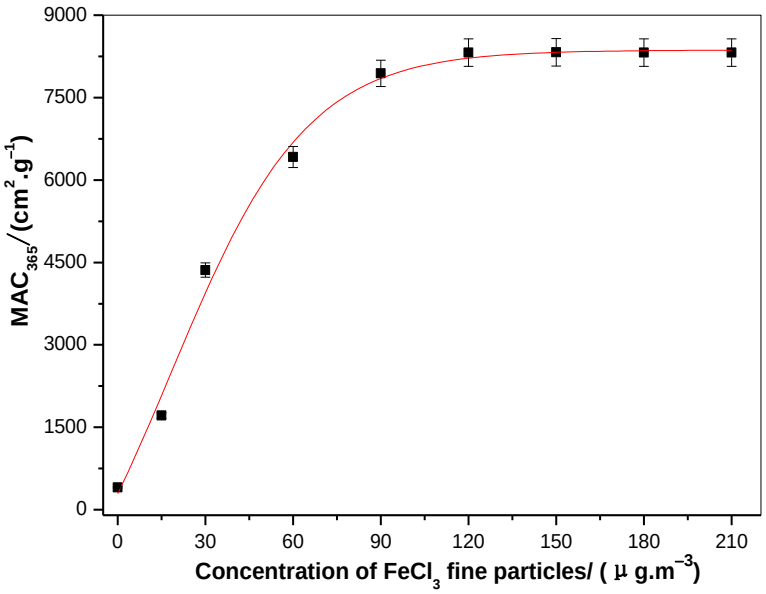


Figure 13. *MAC* at 365 nm (MAC_{365}) of toluene SOA under different concentrations of ferric chloride fine particles.

When ferric chloride fine particles are present in the reaction system, <*MAC*> and MAC_{365} of toluene SOA particles increase obviously and gradually with a rising concentration of fine particles. When the concentration of ferric chloride fine particles is 120 μg·m^{-3}, <*MAC*> of toluene SOA is 420 cm^2·g^{-1} (Figure 12), which is greater than <*MAC*> of ammonia-aging SOA reported by Updyke et al. [40] (300 cm^2·g^{-1}), and is 136% higher than that without fine particles (178 cm^2·g^{-1}). In addition, MAC_{365} of toluene SOA in the presence of 120 μg·m^{-3} ferric chloride fine particles is 8328 cm^2·g^{-1} (Figure 13), which is close to the upper limit value of MAC_{365} for WSOC (2000–11,000 cm^2·g^{-1}) measured by Kirillova et al. [44], and approximately 20 times that without fine particles (407 cm^2·g^{-1}).

This is mainly because high concentration of ferric chloride fine particles can provide more specific surface area and reaction sites, which is conducive to the condensation

and reaction of more gaseous methylcatechol, which reacts with iron ion to form more metallo-organic complexes and methylbenzoquinones, as shown in Figure 10. Compared with metylcatechol and carbonyl compounds, methylbenzoquinones contain more double bonds and thus have greater light absorption capacity [43]. In addition, methylcatechol iron (III) ion and other metallo-organic complex ions have strong light absorption ability [30], so the light absorption ability of particles is significantly enhanced. It is worth noting that <*MAC*> and MAC_{365} of SOA do not increase further when the concentration of ferric chloride fine particles is greater than 120 $\mu g \cdot m^{-3}$. The concentrations of ozone and toluene remained constant in this study, resulting in a certain amount of gaseous methylcatechol for each experiment. When fine particles rise to a certain concentration (120 $\mu g \cdot m^{-3}$), most of the gaseous methylcatechol is converted to form metallo-organic complexes and methylbenzoquinone products. Following that, the concentration of ferric chloride fine particles continues to increase, while metallo-organic complexes and benzoquinone products no longer increase significantly, meaning the chemical components and optics of SOA tend to be stable.

It is worth noting that Dhulipala et al. carried out experimental studies on the generation of SOA via chlorine-initiated oxidation of toluene, and they found that the reaction rate of Cl and toluene was higher than that of OH radicals and toluene [63]. The oxidation of toluene induced by Cl radicals mainly occurs through a methyl hydrogen extraction reaction, producing benzoquinone, benzoic acid and other ring-retaining products, thus affecting the chemical components of atmospheric SOA in coastal areas and other regions with high chlorine content [63]. For comparison with the experiment of Dhulipala et al. [63], in this study, the effect of ferric chloride fine particles on the chemical components of toluene SOA was investigated using an ALTOFMS, UV-Vis absorption spectrometer and electrospray ionization mass spectrometer. It was found that methylcatechol and other gaseous products formed from the OH-initiated oxidation of toluene can condense on the hygroscopic surface of ferric chloride fine particles and undergo a complex reaction to generate metallo-organic complexes with strong light absorption ability. In addition, a high concentration of ferric chloride fine particles can provide more specific surface area and reaction sites, which are conducive to the condensation and reaction of gaseous methylcatechol to form more metallo-organic complexes.

It should be pointed out that the concentration of ferric chloride fine particles used in the chamber study is three orders of magnitude higher than the typical ambient concentration in the air. Nevertheless, the effect of a high concentration of ferric chloride fine particles may be expected to occur in atmospheric conditions since there is evaporation of the aqueous phase, such as liquid aerosol particles, rain and cloud droplets, under which conditions the concentration of iron ion is relatively high [31]. As reviewed by Al-Abadleh, the concentration of dissolved Fe (III) in cloud droplets could be as high as 10 mM [31]. Especially in regions with serious pollution from fine particles of metal and automobile exhaust, under high humidity conditions, methylcatechol and other gaseous products formed from photooxidation of toluene and other aromatic compounds may condense on the surface of liquid aerosol containing iron ions, and they may form metallo-organic complexes with high toxicity and strong light absorption ability, thus changing the chemical composition and optical properties of atmospheric SOA. Our results provide experimental references for studies on the formation and optics of metallo-organic complexes in atmospheric aerosol particles in regions experiencing high levels of fine particles of metal and automobile exhaust pollution, and they may serve as beneficial references for designing chamber experiments involving fine particles of metal.

4. Conclusions

Ferric chloride fine particles from brake wear and other anthropogenic sources are common metal particles in atmosphere, whcih can interact with VOCs via complexing and oxidation–reduction. In this study, the constituents of toluene SOA particles without and with ferric chloride fine particles were characterized by an ALTOFMS, UV-Vis

absorption spectrometer and electrospray ionization mass spectrometer. It was found that methylcatechol and other phenolic compounds and carbonyl compounds such as glyoxal are the main components of toluene SOA particles without ferric chloride fine particles. These constituent molecules only have C=O and C=C double bonds, do not contain strong chromophores or auxochromes and have weak light absorption ability with small <*MAC*> and MAC_{365}. However, when ferric chloride fine particles exist in the system, gaseous methylcatechol can undergo complexation and a redox reaction with iron ion on the surface of fine particles, resulting in metallo-organic complex ions such as dichloro-methylcatechol iron (III) ion and dimethylcatechol iron (III) ion, along with methylbenzoquinone products. <*MAC*> and MAC_{365} of toluene SOA increase obviously due to the strong light absorption ability of these products, and they progressively increase with a rising concentration of ferric chloride. Nevertheless, limitations of the study due to using concentrations of reactants much higher than the ambient ones. In addition, metallo-organic complexes and other products were generated under certain relative humidity conditions, and *MAC* of SOA was measured using an off-line method. Thus, subsequent experiments should be performed to study the influence of relative humidity on the formation of metallo-organic complexes, as well as to conduct on-line measurement of the extinction and scattering coefficient and other optical parameters of SOA.

Author Contributions: Conceptualization, M.H. and W.Z. (Weijun Zhang); methodology, W.Z. (Weijun Zhang) and X.G.; software, X.G. and C.H.; validation, M.H. and W.Z. (Weijun Zhang); formal analysis, W.Z. (Weixiong Zhao); data curation, W.W.; writing—original draft preparation, W.W. and H.H.; writing—review and editing, M.H.; project administration, M.H.; funding acquisition, M.H. All authors have read and agreed to the published version of the manuscript.

Funding: This work is supported by the Key Project of the Natural Science Foundation of Fujian Province of China (No. 2020J02044), the National Natural Science Foundation of China (Nos. 42275136, 41575118) and the Natural Science Foundation of Fujian Province of China (No. 2021J01987).

Institutional Review Board Statement: Not applicable.

Informed Consent Statement: Not applicable.

Data Availability Statement: Not applicable.

Acknowledgments: The authors thank Michael Nusbaum from the Department of English, Xiamen University, Tan Kah Kee College for his language edits. The authors also express our gratitude to the referees for their valuable comments.

Conflicts of Interest: The authors declare no conflict of interest.

References

1. Partha, D.B.; Cassidy-Bushrow, A.E.; Huang, Y.X. Global preterm births attributable to BTEX (benzene, toluene, ethylbenzene, and xylene) exposure. *Sci. Total Environ.* **2022**, *838*, 156390. [CrossRef]
2. Bian, Y.; Zhang, Y.; Zhou, Y.; Feng, X.S. BTEX in the environment: An update on sources, fate, distribution, pretreatment, analysis, and removal techniques. *Chem. Eng.J.* **2022**, *435*, 134825.
3. Behnami, A.; Jafari, N.; Benis, K.Z.; Fanaei, F.; Abdolahnejad, A. Spatio-temporal variations, ozone and secondary organic aerosol formation potential, and health risk assessment of BTEX compounds in east of Azerbaijan Province, Iran. *Urban Clim.* **2023**, *47*, 101360. [CrossRef]
4. Al-Naiema, I.M.; Offenberg, J.H.; Madler, C.J.; Lewandowski, M.; Stone, E.A. Secondary organic aerosols from aromatic hydrocarbons and their contribution to fine particulate matter in Atlanta, Georgia. *Atmos. Environ.* **2020**, *223*, 223. [CrossRef]
5. Lewis, A.C. The changing face of urban air pollution. *Science* **2018**, *359*, 744–745. [CrossRef]
6. Moise, T.; Flores, J.M.; Rudich, Y. Optical properties of secondary organic aerosols and their changes by chemical processes. *Chem. Rev.* **2015**, *115*, 4400–4439. [CrossRef]
7. Fang, Z.; Li, C.L.; He, Q.F.; Czech, H.; Gröger, T.; Zeng, J.Q.; Fang, H.; Xiao, S.X.; Pardo, M.; Hartner, E.; et al. Secondary organic aerosols produced from photochemical oxidation of secondarily evaporated biomass burning organic gases: Chemical composition, toxicity, optical properties, and climate effect. *Environ. Int.* **2021**, *157*, 106801. [CrossRef]
8. Qi, X.; Zhu, S.P.; Zhu, C.Z.; Hu, J.; Lou, S.R.; Xu, L.; Dong, J.G.; Cheng, P. Smog chamber study of the effects of NO*x* and NH_3 on the formation of secondary organic aerosols and optical properties from photo-oxidation of toluene. *Sci. Total Environ.* **2020**, *727*, 138632. [CrossRef]

9. Babar, Z.B.; Park, J.H.; Lim, H.J. Influence of NH_3 on secondary organic aerosols from the ozonolysis and photooxidation of α-pinene in a flow reactor. *Atmos. Environ.* **2017**, *164*, 71–84. [CrossRef]
10. Liu, S.J.; Huang, D.D.; Wang, Y.Q.; Zhang, S.; Liu, X.D.; Wu, C.; Du, W.; Wang, G.H. Synergetic effects of NH_3 and NO*x* on the production and optical absorption of secondary organic aerosol formation from toluene photooxidation. *Atmos. Chem. Phys.* **2021**, *21*, 17759–17773. [CrossRef]
11. Chowdhury, P.H.; He, Q.F.; Male, T.L.; Brune, W.H.; Rudich, Y.; Pardo, M. Exposure of lung epithelial cells to photochemically aged secondary organic aerosol shows increased toxic effects. *Environ. Sci. Tech. Let.* **2018**, *5*, 424–430. [CrossRef]
12. Kim, S.J.; Lee, S.J.; Lee, H.Y.; Son, J.M.; Lim, H.B.; Kim, H.W.; Shin, H.J.; Ji, Y.L.; Choi, S.D. Characteristics of volatile organic compounds in the metropolitan city of Seoul, South Korea: Diurnal variation, source identification, secondary formation of organic aerosol, and health risk. *Sci. Total Environ.* **2022**, *838*, 156344. [CrossRef]
13. Guan, Q.Y.; Li, F.C.; Yang, L.Q.; Zhao, R.; Yang, Y.Y.; Luo, H.P. Spatial-temporal variations and mineral dust fractions in particulate matter mass concentrations in an urban area of northwestern China. *J. Environ. Manag.* **2018**, *222*, 95–103. [CrossRef]
14. Deguillaume, L.; Leriche, M.; Desboeufs, K.; Mailhot, G.; George, C.; Chaumerliac, N. Transition metals in atmospheric liquid phases: Sources, reactivity, and sensitive parameters. *Chem. Rev.* **2005**, *105*, 3388–3431. [CrossRef]
15. Tang, M.J.; Cziczo, D.J.; Grassian, V.H. Interactions of water with mineral dust aerosol: Water adsorption, hygroscopicity, cloud condensation, and ice nucleation. *Chem. Rev.* **2016**, *116*, 4205–4259. [CrossRef]
16. Gao, Y.; Ji, H.B. Microscopic morphology and seasonal variation of health effect arising from heavy metals in $PM_{2.5}$ and PM_{10}: One-year measurement in a densely populated area of urban Beijing. *Atmos. Res.* **2018**, *212*, 213–226. [CrossRef]
17. Hochella, M.F., Jr.; Lower, S.K.; Maurice, P.A.; Penn, R.L.; Sahai, N.; Sparks, D.L.; Twining, B.S. Nanominerals, mineral nanoparticles, and earth systems. *Science* **2008**, *319*, 1631–1635. [CrossRef]
18. Tang, M.J.; Huang, X.; Lu, K.D.; Ge, M.F.; Li, Y.J.; Cheng, P.; Zhu, T.; Ding, A.J.; Zhang, Y.H.; Gligorovski, S.; et al. Heterogeneous reactions of mineral dust aerosol: Implications for tropospheric oxidation capacity. *Atmos. Chem. Phys.* **2017**, *17*, 11727–11777. [CrossRef]
19. Babar, Z.B.; Park, J.H.; Kang, J.; Lim, H.J. Characterization of a smog chamber for studying formation and physicochemical properties of secondary organic aerosol. *Aerosol Air Qual. Res.* **2016**, *16*, 3102–3113. [CrossRef]
20. Shao, Y.Q.; Wang, Y.; Du, M.; Voliotis, A.; Alfarra, M.R.; O'Meara, S.P.; Turner, S.F.; McFiggans, G. Characterization of the Manchester aerosol chamber facility. *Atmos. Meas. Tech.* **2022**, *15*, 539–559. [CrossRef]
21. Chu, B.W.; Chen, T.Z.; Liu, Y.C.; Ma, Q.X.; Mu, Y.J.; Wang, Y.H.; Ma, J.Z.; Zhang, P.; Liu, J.; Liu, C.S.; et al. Application of smog chambers in atmospheric process studies. *Natl. Sci. Rev.* **2022**, *9*, 126–141. [CrossRef] [PubMed]
22. Chu, B.W.; Hao, J.M.; Takekawa, H.; Li, J.H.; Wang, K.; Jiang, J.K. The remarkable effect of $FeSO_4$ seed aerosols on secondary organic aerosol formation from photooxidation of α-pinene/NO*x* and toluene/ NO*x*. *Atmos. Environ.* **2012**, *55*, 26–34. [CrossRef]
23. Chu, B.W.; Liu, Y.C.; Li, J.H.; Takekawa, H.; Liggio, J.; Li, S.M.; Jiang, J.K.; Hao, J.M.; He, H. Decreasing effect and mechanism of $FeSO_4$ seed particles on secondary organic aerosol in α-pinene photooxidation. *Environ. Pollut.* **2014**, *193*, 88–93. [CrossRef]
24. Chu, B.W.; Liggio, J.; Liu, Y.C.; He, H.; Takekawa, H.; Li, S.M.; Hao, J.M. Influence of metal-mediated aerosol-phase oxidation on secondary organic aerosol formation from the ozonolysis and OH-oxidation of α-pinene. *Sci. Rep.* **2016**, *7*, 40311. [CrossRef] [PubMed]
25. Scheinhardt, S.; Müller, K.; Spindler, G.; Herrmann, H. Complexation of trace metals in size-segregated aerosol particles at nine sites in Germany. *Atmos. Environ.* **2013**, *74*, 102–109. [CrossRef]
26. Furukawa, T.; Takahashi, Y. Oxalate metal complexes in aerosol particles: Implications for the hygroscopicity of oxalate-containing particles. *Atmos. Chem. Phys.* **2011**, *11*, 4289–4301. [CrossRef]
27. Singh, D.K.; Gupta, T. Role of transition metals with water soluble organic carbon in the formation of secondary organic aerosol and metallo-organics in PM_1 sampled during post monsoon and pre-winter time. *J. Aerosol Sci.* **2016**, *94*, 56–69. [CrossRef]
28. Singh, D.K.; Gupta, T. Role of ammonium ion and transition metals in the formation of secondary organic aerosol and metallo-organic complex within fog processed ambient deliquescent submicron particles collected in central part of Indo-Gangetic Plain. *Chemosphere* **2017**, *181*, 725–737. [CrossRef]
29. Moretti, S.; Smets, W.; Hofman, J.; Mubiana, K.V.; Oerlemans, E.; Vandenheuvel, D.; Samson, R.; Blust, R.; Lebeer, S. Human inflammatory response of endotoxin affected by particulate matter-bound transition metals. *Environ. Pollut.* **2019**, *244*, 118–126. [CrossRef]
30. Kodikara, M.S.; Stranger, R.; Humphrey, M.G. Computational studies of the nonlinear optical properties of organometallic complexes. *Coordin. Chem. Rev.* **2019**, *375*, 389–409. [CrossRef]
31. Al-Abadleh, H.A. Aging of atmospheric aerosols and the role of iron in catalyzing brown carbon formation. *Environ. Sci. Atmos.* **2021**, *1*, 297–345. [CrossRef]
32. Tian, H.Z.; Zhu, C.Y.; Gao, J.J.; Cheng, K.; Hao, J.M.; Wang, K.; Hua, S.B.; Wang, Y.; Zhou, J.R. Quantitative assessment of atmospheric emissions of toxic heavy metals from anthropogenic sources in China: Historical trend, spatial distribution, uncertainties, and control policies. *Atmos. Chem. Phys.* **2015**, *15*, 10127–10147. [CrossRef]
33. Zhang, M.Y.; Shao, L.Y.; Jones, T.; Feng, X.L.; Ge, S.Y.; Yang, C.X.; Cao, Y.X.; BéruBé, K.; Zhang, D.Z. Atmospheric iron particles in $PM_{2.5}$ from a subway station, Beijing, China. *Atmos. Environ.* **2022**, *283*, 119175. [CrossRef]
34. Huang, M.Q.; Zhang, W.J.; Wang, Z.Y.; Fang, L.; Kong, R.H.; Shan, X.B.; Liu, F.Y.; Sheng, L.S. Mass spectrometry study of OH-initiated photooxidation of toluene. *Chin. J. Chem. Phys.* **2011**, *24*, 672–678. [CrossRef]

35. Huang, M.Q.; Hao, L.Q.; Gu, X.J.; Hu, C.J.; Zhao, W.X.; Wang, Z.Y.; Fang, L.; Zhang, W.J. Effects of inorganic seed aerosols on the growth and chemical composition of secondary organic aerosol formed from OH-initiated oxidation of toluene. *J. Atmos. Chem.* **2013**, *70*, 151–164. [CrossRef]
36. Lu, T.T.; Huang, M.Q.; Zhao, W.X.; Hu, C.J.; Gu, X.J.; Zhang, W.J. Influence of ammonium sulfate seed particle on optics and compositions of toluene derived organic aerosol in photochemistry. *Atmosphere* **2020**, *11*, 961. [CrossRef]
37. Huang, M.Q.; Hao, L.Q.; Cai, S.Y.; Gu, X.J.; Zhang, W.X.; Hu, C.J.; Wang, Z.Y.; Fang, L.; Zhang, W.J. Effects of inorganic seed aerosols on the particulate products of aged 1,3,5-trimethylbenzene secondary organic aerosol. *Atmos. Environ.* **2017**, *152*, 490–502. [CrossRef]
38. Assaf, E.; Fittschen, C. Cross section of OH radical overtone transition near 7028 cm^{-1} and measurement of the rate constant of the reaction of OH with HO_2 radicals. *J. Phys. Chem. A* **2016**, *120*, 7051–7059. [CrossRef]
39. Carlton, A.G.; Turpin, B.; Altieri, K.E.; Seitzinger, S.; Reff, A.; Lim, H.-J.; Ervens, B. Atmospheric oxalic acid and SOA production from glyoxal: Results of aqueous photooxidation experiments. *Atmos. Environ.* **2007**, *41*, 7588–7602. [CrossRef]
40. Updyke, K.M.; Nguyen, T.B.; Nizkorodov, S.A. Formation of brown carbon via reactions of ammonia with secondary organic aerosols from biogenic and anthropogenic precursors. *Atmos. Environ.* **2012**, *63*, 22–31. [CrossRef]
41. Powelson, M.H.; Espelien, B.M.; Hawkins, L.N.; Galloway, M.M.; De Haan, D.O. Brown carbon formation by aqueous-phase carbonyl compound reactions with amines and ammonium sulfate. *Environ. Sci. Technol.* **2014**, *48*, 985–993. [CrossRef]
42. Lin, X.; Huang, M.Q.; Lu, T.T.; Zhao, W.X.; Hu, C.J.; Gu, X.J.; Zhang, W.J. Characterization of imidazole compounds in aqueous secondary organic aerosol generated from evaporation of droplets containing pyruvaldehyde and inorganic ammonium. *Atmosphere* **2022**, *13*, 970. [CrossRef]
43. Laskin, A.; Laskin, J.; Nizkorodov, S.A. Chemistry of atmospheric brown carbon. *Chem. Rev.* **2015**, *115*, 4335–4382. [CrossRef] [PubMed]
44. Kirillova, E.N.; Andersson, A.; Han, J.; Lee, M.; Gustafsson, Ö. Sources and light absorption of water-soluble organic carbon aerosols in the outflow from northern China. *Atmos. Chem. Phys.* **2014**, *14*, 1413–1422. [CrossRef]
45. Liu, J.M.; Scheuer, E.; Dibb, J.; Ziemba, L.D.; Thornhill, K.L.; Anderson, B.E.; Wisthaler, A.; Mikoviny, T.; Devi, J.J.; Bergin, M.; et al. Brown carbon in the continental troposphere. *Geophys. Res. Lett.* **2014**, *41*, 2191–2195. [CrossRef]
46. Liu, J.; Bergin, M.; Guo, H.; King, L.; Kotra, N.; Edgerton, E.; Weber, R.J. Size-resolved measurements of brown carbon in water and methanol extracts and estimates of their contribution to ambient fine-particle light absorption. *Atmos. Chem. Phys.* **2013**, *13*, 12389–12404. [CrossRef]
47. Shetty, N.J.; Pandey, A.; Baker, S.; Hao, W.M.; Chakrabarty, R.K. Measuring light absorption by freshly emitted organic aerosols: Optical artifacts in traditional solvent-extraction- based methods. *Atmos. Chem. Phys.* **2019**, *19*, 8817–8830. [CrossRef]
48. Liu, S.J.; Liu, X.D.; Wang, Y.Q.; Zhang, S.; Wu, C.; Du, W.; Wang, G.H. Effect of NO*x* and RH on the secondary organic aerosol formation from toluene photooxidation. *J. Environ. Sci. China* **2022**, *114*, 1–9. [CrossRef]
49. Li, Y.X.; Zhao, J.Y.; Wang, Y.; Seinfeld, J.H.; Zhang, R.Y. Multigeneration production of secondary organic aerosol from toluene photooxidation. *Environ. Sci. Technol.* **2021**, *55*, 8592–8603. [CrossRef]
50. White, S.J.; Jamie, I.M.; Angove, D.E. Chemical characterisation of semi-volatile and aerosol compounds from the photooxidation of toluene and NO*x*. *Atmos. Environ.* **2014**, *83*, 237–244. [CrossRef]
51. Dong, Z.K.; Tang, R.Y.; Liu, H.F.; Zhang, Q.Z.; Zong, W.S.; Cheng, J.M.; Shi, X.L. The formation mechanism of highly oxygenated organic molecules produced by toluene in the urban atmosphere. *Atmos. Environ.* **2023**, *295*, 119555. [CrossRef]
52. Ji, Y.M.; Zhao, J.; Terazono, H.; Terazono, H.; Misawa, K.; Levitt, N.; Li, Y.X.; Lin, Y.; Peng, J.F.; Wang, Y.; et al. Reassessing the atmospheric oxidation mechanism of toluene. *Proc. Natl. Acad. Sci. USA* **2017**, *114*, 8169–8174. [CrossRef]
53. Suh, I.; Zhang, R.; Molina, L.T.; Molina, M.J. Oxidation mechanism of aromatic peroxy and bicyclic radicals from OH-toluene reactions. *J. Am. Chem. Soc.* **2003**, *125*, 12655–12665. [CrossRef]
54. Sato, K.; Takami, A.; Kato, Y.; Seta, T.; Fujitani, Y.; Hikida, T.; Shimono, A.; Imamura, T. AMS and LC/MS analyses of SOA from the photooxidation of benzene and 1,3,5-trimethyl benzene in the presence of NO*x*: Effects of chemical structure on SOA aging. *Atmos. Chem. Phys.* **2012**, *12*, 4667–4682. [CrossRef]
55. Sato, K.; Takami, A.; Isozaki, T.; Hikida, T.; Shimono, A.; Imamura, T. Mass spectrometric study of secondary organic aerosol formed from the photo-oxidation of aromatic hydrocarbons. *Atmos. Environ.* **2010**, *44*, 1080–1087. [CrossRef]
56. Marković, S.; Tošović, J. Application of time-dependent density functional and natural bond orbital theories to the UV–vis absorption spectra of some phenolic compounds. *J. Phys. Chem. A* **2015**, *119*, 9352–9362. [CrossRef]
57. Arndt, J.; Deboudt, K.; Anderson, A.; Blondel, A.; Eliet, S.; Flament, P.; Fourmentin, M.; Healy, R.M.; Savary, V.; Setyan, A.; et al. Scanning electron microscopy-energy dispersive X-ray spectrometry (SEM-EDX) and aerosol time-of-flight mass spectrometry (ATOFMS) single particle analysis of metallurgy plant emissions. *Environ. Pollut.* **2016**, *210*, 9–17. [CrossRef]
58. Rizvi, M.A.; Mane, M.; Khuroo, M.A.; Peerzada, G.M. Computational survey of ligand properties on iron(III)–iron(II) redox potential: Exploring natural attenuation of nitroaromatic compounds. *Monatsh. Chem.* **2017**, *148*, 655–668. [CrossRef]
59. Albarran, G.; Boggess, W.; Rassolov, V.; Schuler, R.H. Absorption spectrum, mass spectrometric properties, and electronic structure of 1,2-benzoquinone. *J. Phys. Chem. A* **2010**, *114*, 7470–7478. [CrossRef]
60. Powell, H.K.J.; Taylor, M.C. Interactions of iron(II) and iron(III) with gallic acid and its homologues: A potentiormetric and spectrophotometric study. *Aust. J. Chem.* **1982**, *35*, 739–756. [CrossRef]

61. Slikboer, S.; Grandy, L.; Blair, S.L.; Nizkorodov, S.A.; Smith, R.W.; Al-Abadleh, H.A. Formation of light absorbing soluble secondary organics and insoluble polymeric particles from the dark reaction of catechol and guaiacol with Fe(III). *Environ. Sci. Technol.* **2015**, *49*, 7793–7802. [CrossRef] [PubMed]
62. Zhu, Z.H.; Zhang, J.; Lv, G.C.; George, C.; Herrmann, H.; Fu, H.B.; Li, D.; Zhang, L.W.; Sun, X.M.; Sun, H.; et al. Complexation of Fe(III)/Catechols in atmospheric aqueous phase and the consequent cytotoxicity assessment in human bronchial epithelial cells (BEAS-2B). *Ecotoxicol. Environ. Saf.* **2020**, *202*, 110898. [CrossRef] [PubMed]
63. Dhulipala, S.V.; Bhandari, S.; Hildebrandt Ruiz, L. Formation of oxidized organic compounds from Cl-initiated oxidation of toluene. *Atmos. Environ.* **2019**, *199*, 265–273. [CrossRef]

Disclaimer/Publisher's Note: The statements, opinions and data contained in all publications are solely those of the individual author(s) and contributor(s) and not of MDPI and/or the editor(s). MDPI and/or the editor(s) disclaim responsibility for any injury to people or property resulting from any ideas, methods, instructions or products referred to in the content.